Corrosion Science 227 (2024) 111734

Contents lists available at ScienceDirect

Corrosion Science

journal homepage: www.elsevier.com/locate/corsci

# The effect of Fe-anion interactions on corrosion of ferrous surfaces by phosphonium ionic liquids

Ting Liu [a,1], Md Hafizur Rahman [b,1], Pradeep L. Menezes [b], Ashlie Martini [a,*]

[a] Department of Mechanical Engineering, University of California Merced, 5200 Lake Rd, Merced, 95343, CA, USA
[b] Department of Mechanical Engineering, University of Nevada Reno, 1664 N Virginia St, 89557, Reno, NV, USA

ARTICLE INFO

*Keywords:*
Ionic liquids
Pitting corrosion
Reactive molecular dynamics
Adsorption mechanisms

ABSTRACT

Experiments and simulations were used to investigate interactions between ferrous surfaces and trihexyltetradecylphosphonium benzoate or salicylate. Differences between the ionic liquids were observed in open circuit potential, potentiodynamic polarization, cyclic potentiodynamic polarization, electrochemical impedance spectroscopy, and long-duration corrosion tests. While both ionic liquids were far less corrosive than water, salicylate exhibited slower charge transfer and lower surface protection potential than benzoate. These observations were analyzed using simulations of chemical reactions between ions and an ideal Fe(100) surface. Simulation results showed that salicylate and benzoate differed in their bonding configurations and orientations, suggesting distinct adsorption mechanisms for these similar ionic liquids.

## 1. Introduction

Room temperature ionic liquids (ILs) are a class of organic salts that are liquid at ambient temperature [1,2]. ILs have many advantages compared to conventional organic compounds in terms of chemical, physical, thermal, and biological properties [2,3]. For example, ILs have high thermal and chemical stability [3–5] and low vapor pressure [6]. Some ILs are also miscible in both water and oil [7–9]. There are anions, such as salicylate, benzoate, and saccharinate, that can be extracted from plants [10] and numerous studies have investigated ILs that can be recycled and reused without volume loss [11–15]. Therefore, ILs are considered to be promising green engineering liquids that offer a potential solution to challenges associated with both solvent emission and catalytic recycling [16,17]. These advantages make ILs useful for a diverse range of applications such as lubricants, battery electrolytes, heat transfer fluids, solvents for coating materials, additives in polymeric materials, and more [2–4,10,18–23].

In many applications, ILs are in direct contact with a metal surface and form a solid–liquid interface. In such cases, ILs have been found to form adsorption layers composed of cations, anions, and their decomposition products. The adsorption layers can have either a corrosive or protective effect, depending on the combination of IL and metal, as well as on temperature [24]. ILs are usually less corrosive than typical oxidizing species like neutral sodium chloride solution, acidic or alkaline solution, and oxygen [25–33], so they can be used as corrosion inhibitors for metal surfaces like carbon steel, stainless steel, magnesium, copper, and zinc [20,34–37]. However, many ILs are highly polar and have low vapor pressures, and therefore can be more corrosive to metal surfaces than traditional organic solvents [2,38]. Generally, corrosion is a concern because it can reduce the strength and durability of equipment and structures [38,39]. To minimize corrosion in applications involving ILs, it is important to understand the mechanisms by which ILs interact with and affect corrosion of metal surfaces.

There have been a number of experimental studies that have examined the corrosion of metals in contact with ILs. The rate of corrosion of metals interacting with ILs has been measured by the weight loss method using a rotating cage experiment [38,40,41]. Electrochemical tests, like corrosion potential, corrosion current density, and electrochemical impedance spectroscopy, have also been applied to measure corrosivity of ILs [25,40–44]. Such studies reported that corrosion processes were controlled by charge transfer at the metal/IL interface [25,41,42,45] and the corrosivity of ILs strongly depends on the surface material and morphology, the presence of impurities, and the temperature [25,38–43,46,47]. Corrosion of metals by ILs has also been shown to be affected by the chemical nature of the IL cation and anion [24,25,38,39,43,44,47,48].

The cation can affect the way that ILs interact with metal surfaces and, therefore, the corrosion of the metal [24,44,47,48]. For example, (2-hydroxyethyl)-trimethyl-ammonium bistriflimide (choline

* Corresponding author.
*E-mail address:* amartini@ucmerced.edu (A. Martini).
[1] Joint first-author, the two authors contributed equally to this paper.

https://doi.org/10.1016/j.corsci.2023.111734
Received 20 July 2023; Received in revised form 10 November 2023; Accepted 28 November 2023
Available online 29 November 2023

NTF2) caused less corrosion of a copper surface than butyl-trimethylammonium NTF2 [24]. The incorporation of a hydroxyl group into the cation alkyl side chain was found to decrease corrosivity [42]. Electrochemical tests showed that protic ILs had a narrower electrochemical stability window and were generally more reactive towards metals than aprotic ILs [44]. Corrosion of aluminium and copper in imidazolium-based ILs with different alkyl chain lengths showed that corrosion decreased with increasing alkyl chain length [47]. For steel surfaces, alkyl substituents like polar groups, fragments, conjugated bonds, and various heteroatoms in the cation structure led to lower corrosion rate due to the improved adsorption of cations on the surface [48].

It has also been reported that the anion moiety plays the dominant role in corrosion of metal surfaces [43,44,49,50] since the polarization behavior of ILs is mainly governed by anions [43]. For example, anions like tosylate and dimethyl phosphate generally had higher corrosivity on carbon steel and aluminium than ethyl sulfate, octyl sulfate, and chloride [38]. Severe corrosion on iron based alloys was found for choline methanesulfonate while choline NTF2 exhibited significantly lower corrosiveness [42]. On copper surfaces, 1-ethyl-3-methylimidazolium phosphonate ([EMIM][$EtPO_3H$]) showed more corrosion than 1-ethyl-3-methylimidazolium octylsulfate ([EMIM][$C_8H_{17}SO_4$]) due to the formation of a soluble phosphonate-copper complex. Also, 1-hexyl-3-methylimidazolium tetrafluoroborate ([HMIM][$BF_4$]) showed more corrosion than 1-hexyl-3-methylimidazolium hexafluorophosphate ([HMIM][$PF_6$]) since the [$BF_4$] anion formed a soluble species with copper while the [$PF_6$] anion formed a uniform protective layer on the copper surface [49]. ILs composed of strongly coordinating anions such as bis(trifluoromethylsulfonyl)imide (TFSI) are more corrosive to metal surfaces than chloroaluminate ILs or ILs with weakly coordinating anions such as tetrafluoroborate ($BF_4$) and hexafluorophosphate ($PF_6$) because TFSI can facilitate metal dissolution by forming a tight solvation layer with dissolved metal ions [39].

Results reported so far have shown that the chemical nature of the ions can affect the corrosion of metal surfaces interacting with ILs and that the anion plays a key role. However, the mechanisms by which anions affect metal corrosion are still not fully understood. Here, we focused on phosphonium-based ILs that are used in various applications where they come into contact with ferrous materials [10,22,51,52]. We specifically studied trihexyltetradecylphosphonium benzoate ([P6,6,6,14][Benz]) and trihexyltetradecylphosphonium salicylate ([P6,6,6,14][Sali]). These ILs have been used as lubricants for stainless steel [53] and the anions are derived from natural organic sources [10]. [P6,6,6,14][Benz] and [P6,6,6,14][Sali] were also chosen because they have the same cation but slightly different anions, which enabled isolation of the effect of the anion. First, we characterized corrosion of steel in the presence of phophonium ILs experimentally. Then, we used reactive molecular dynamics (MD) simulations to investigate ion-surface interactions and reactions to identify and understand differences between the two anions.

## 2. Methods

### 2.1. Corrosion experiments

The two ILs, [P6,6,6,14][Benz] and [P6,6,6,14][Sali] were synthesized using trihexyltetradecylphosphonium chloride and sodium benzoate, or sodium salicylate through ion exchange reaction of trihexyl tetradecyl phosphonium chloride and sodium benzoate/salicylate, as reported in previous literature [10,14,54]. The produced ILs were dried at 80° C, under vacuum for at least 6 h and Fourier Transform Infrared Spectroscopy (FTIR) analysis was done to confirm the absence of any water peak. The dried ILs were kept at room temperature inside a humidity-controlled desiccator (10 ± 5%RH) before use. Atomic representations of the individual ions are shown in Fig. 1.

The chemical structures of the ILs were characterized using FTIR and $^1$H Nuclear Magnetic Resonance (NMR) spectroscopy. FTIR analyses were performed using a Nicolet FTIR (Model: iS™ 380, Thermo Scientific). $^1$H NMR analysis of the neat ILs was carried out using an Agilent 500-MHz NMR spectroscope. Deuterated chloroform (CDCl3 having D, 99.8%+0.05% V/V TMS) was used as the solvent to carry out the experiments. The results were analyzed using MestReNova software.

FTIR spectra for the two phosphonium ILs are shown in Fig. S1. For both ILs, prominent peaks were observed for alkyl $sp^3$ C–H bonds (2750–3000 $cm^{-1}$) corresponding to the long alkyl chain in the cation, and aromatic C–C bonds (1450–1600 $cm^{-1}$) that are present in the aromatic ring in the anion moieties. Similar spectra for these two ILs were reported previously [54].

Structural confirmation was further obtained from $^1$H NMR analyses. Fig. S2(a) shows the $^1$H NMR spectrum for the [P6,6,6,14][Sali]. Here, eight multiplets (A–H) are observed, among which four (A, B, C and D) are in the aromatic region (6–8 ppm) [55]. The integral value for these four multiplets was four, corresponding to the number of proton nuclei present in the aromatic ring structure of salicylate anion. Among the other four multiplets, F is located in the methyl group region (−1 to 4) and corresponds to the four methyl groups ($–CH_3$) present at the four ends of the cation side chains [55]. E, G, and H multiplets are located within the alkyl chain region (1.1–5.2), confirming the 56 proton nuclei present in the four alkyl chain branches of the cation [55]. This is consistent with results for [P6,6,6,14][Sali] previously reported [54]. Similarly, in Fig. S2(b), the $^1$H spectrum for [P6,6,6,14][Benz] is presented, where 73 proton nuclei are confirmed within the ionic liquid structure, again consistent with literature [54].

To study the corrosion behavior of steel, AISI 52100 steel surfaces were prepared with an average surface roughness (Sa) of 0.16 μm. Open circuit potential (OCP) measurements, potentiodynamic polarization (PDP), and cyclic potentiodynamic polarization (CPDP) scans of the steel specimens were carried out for the neat ILs and for water (as a reference). A three-electrode electrochemical cell connected to a Gamry Reference 1010 potentiostat (Gamry Instruments, Warminster, PA, USA) was used to carry out the OCP, PDP, and CPDP investigations. A standard saturated calomel electrode (SCE) was used as the reference electrode, and a graphite rod was used as the counter electrode. The AISI 52100 steel specimen was used as the working electrode in the three-electrode setup. A 0.315 $cm^2$ surface area of the working electrode was exposed to each liquid ([P6,6,6,14][Benz], [P6,6,6,14][Sali], and water) separately over 60 mins in each OCP test. After this duration, the electrochemical system reached a steady-state potential. At this condition, the PDP tests were carried out for each test liquid at a scan rate of 1 mV/s from an initial voltage of −0.5 V to a final voltage of 1.5 V, with respect to OCP. Similarly, the CPDP tests were carried out at the steady state potential with a 1 mV/s scan rate for [P6,6,6,14][Sali] and [P6,6,6,14][Benz]. Each test was repeated at least twice.

The surface topographies were recorded after the electrochemical tests using a profilometer (Rtec Instruments, CA, USA). Then, to characterize the long-term corrosion behavior of the ILs, AISI 52100 steel samples were submerged in [P6,6,6,14][Benz] or [P6,6,6,14][Sali] for 28 days, and their surface topographies were recorded using the profilometer. To investigate the corrosion mechanisms, Electrochemical Impedance Spectroscopy experiment was carried out using a two-electrode system using the Gamry 1010 potentiostat from an initial frequency of $10^9$ Hz to a final frequency of 0.01 Hz. FTIR scans were also carried out to detect any variation in the IL samples before and after long term corrosion tests. Finally, the corroded surfaces were analyzed using a Renishaw InVia Raman equipment between 200–1400 $cm^{-1}$ wavenumbers.

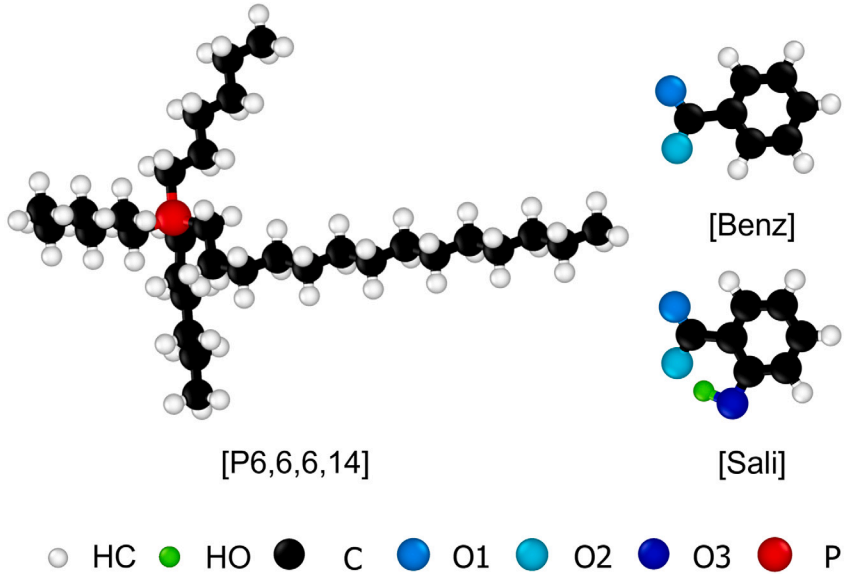


**Fig. 1.** Chemical structures of the [P6,6,6,14] cation, [Benz] anion, and [Sali] anion evaluated in the current study. HC: hydrogen atoms bonded to carbon atoms; HO: hydrogen atoms bonded to oxygen atoms; O1: oxygen type 1 of the carboxyl group; O2: oxygen type 2 of the carboxyl group; O3: oxygen atom in the hydroxyl group.

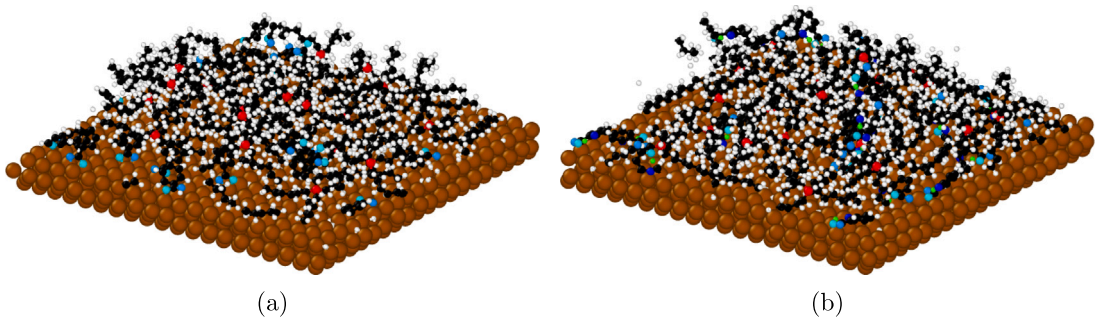


**Fig. 2.** Perspective-view snapshots at the end of the simulations at 300 K for (a) [P6,6,6,14][Benz] and (b) [P6,6,6,14][Sali]. Brown spheres are Fe atoms and other colors are as defined in Fig. 1.

### 2.2. Reactive molecular dynamics simulation

Reactive MD simulations of [P6,6,6,14][Benz] and [P6,6,6,14][Sali] on an ideal 56.8 × 56.8 Å Fe(100) surface were performed to investigate the surface interactions and reactions of these ions. The model system comprised a body-centered cubic Fe(100) slab and 20 ion pairs in a periodic simulation box. Since the two ILs were characterized experimentally at 100% concentration in experiments, the effect of solvent molecules or other impurities on the adsorption process was not modeled. The structures of the individual ions are shown in Fig. 1. The ion models were created by Packmol [56] and 20 ion pairs of either [P6,6,6,14][Benz] or [P6,6,6,14][Sali] were randomly placed 1 nm above the Fe(100) surface. For the crystal structure of ferrous surface, the most commonly used iron surfaces used to mimic ferrous metals in MD simulations are (110), (100) and (001) [57]. All these are simple approximations of steel and here we chose Fe(100) as representative.

All simulations were performed using the open-source Large-scale Atomic/Molecular Massively Parallel Simulator (LAMMPS) package [58]. Simulations were based on the ReaxFF force field. ReaxFF parameters for P/C/H/O were taken from Ref. [59] and parameters for interactions with Fe were taken from Ref. [60]. These force field parameters have undergone extensive validation and benchmarking against experimental data and density functional theory (DFT) calculations. Particularly, parameters for P/C/H/O interactions were reported to give good agreement with DFT energies for C–O bond dissociation, P–C bond dissociation, and C–P–C angle distortion. Additionally, the density of phosphonium glycinate and its mixture with $CO_2$ calculated using the ReaxFF force field matched well with experimental values [59]. Most relevant to the current study, this parameter set was used previously to model thermal decomposition of phosphonium benzoate and phosphonium salicylate with results that agreed well with experimental observations [5]. Parameters for interactions between Fe and P/C/H/O were validated by reproducing energies calculated using DFT for Fe–O–P and Fe–P–O angles, Fe–P bond dissociation, Fe–O–P angle bending, and binding energies for P and PO on an Fe(100) surface [60]. This parameter set was used previously to model thermal decomposition of tricresyl phosphate on ferrous surfaces where simulation-calculated reaction products were consistent with those measured in experiments [61].

After energy minimization, the simulations were performed with a canonical ensemble with a time step of 0.25 fs. The temperature was maintained at 300 K with a damping parameter of 25 fs using a Nosé–Hoover thermostat [62]. During this simulation, the ions approached and reacted with the surface atoms. It was found that the number of ion-surface bonds reached steady-state after about 0.6 ns at 300 K. Therefore, the simulations were performed for a total duration of 1 ns by which time the potential energy of the simulation system and number of bonds had reached steady state. Simulations were also run at 400 K and 500 K for 1 ns. Figs. 2 show snapshots from the end of representative simulations after reactions between the ions and surface reached steady state. Chemical bonding between atoms in ILs and Fe atoms in surface was analyzed based on the ReaxFF bond table using

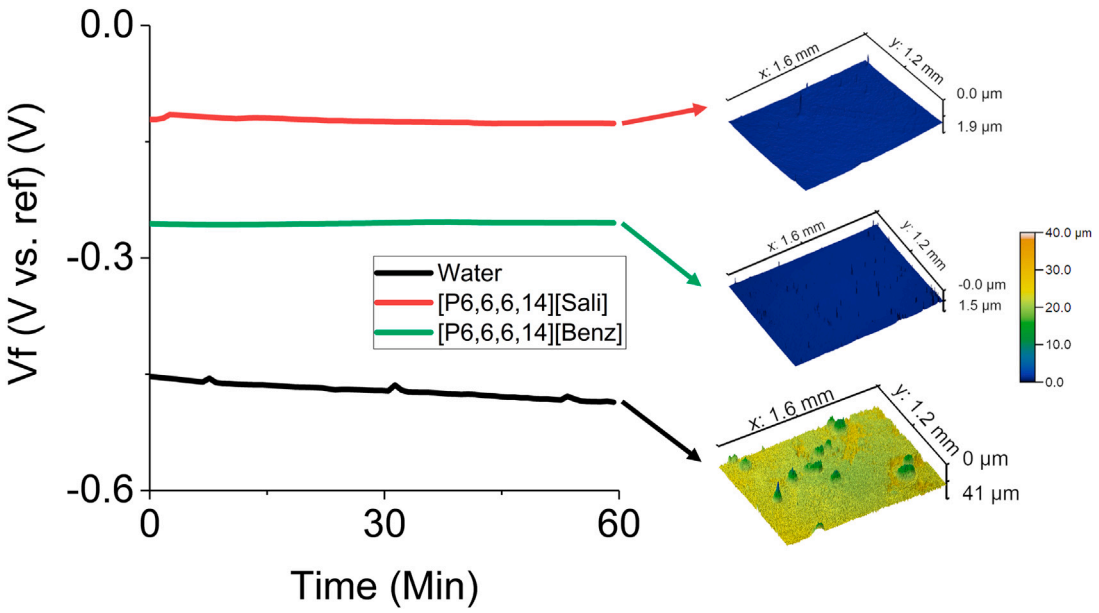


**Fig. 3.** Representative open circuit potential for the two ILs and water. To the right are representative profilometer images of the steel surfaces taken after the tests. The color scale is inverted in the topography images such that large positive values correspond to deep pits. Each test was repeated twice.

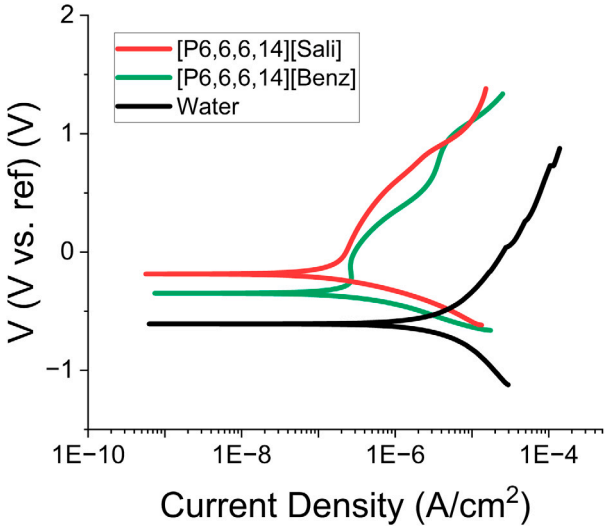


**Fig. 4.** Representative potentiodynamic polarization curves for the two ILs and water. Each test was repeated twice.

user-defined Python scripts. Results were averaged over 20 time frames during the last 25 ps of the simulation.

## 3. Results and discussion

The OCP results for the AISI 52100 steel with the two phosphonium ILs as well as with water for reference are shown in Fig. 3. It has been reported the OCP is a measure of the corrosion potential of electrolytes [63]. Both ILs had much lower corrosion potential than the water. Comparing the two ILs, the stable voltage recorded for [P6,6,6,14][Sali] was −0.12 V and, for [P6,6,6,14][Benz], it was −0.24 V, indicating [Sali] has lower corrosion potential than [Benz]. Profilometer images taken after the electrochemical tests are also shown in Fig. 3. Significant pitting occurred for water whereas, for both ILs, the pitting marks were shallow and small.

The PDP curves of the steel surfaces for the two ILs and water are reported in Fig. 4. These results provide an estimation of relative current flow above OCP and can be used to assess the relative corrosiveness of different electrolytes for a given metal [64]. The corrosion current density was obtained from the polarization curve using the Tafel extrapolation technique [65]. The measured current densities for [P6,6,6,14][Sali], [P6,6,6,14][Benz], and water were 0.12 µA/cm$^2$, 0.30 µA/cm$^2$, and 5.8 µA/cm$^2$, respectively. This shows that the water was much more corrosive than the two ILs.

**Table 1**
Cyclic potentiodynamic polarization analysis.

| ILs | $E_{pit}$ (V) | $E_{corr}$ (V) | $E_p$ (V) | Hysteresis type |
|---|---|---|---|---|
| [P6,6,6,14][Benz] | 0.21 | −0.25 | −0.15 | Negative |
| [P6,6,6,14][Sali] | 0.75 | −0.20 | −0.30 | Positive |

The corrosion rate (mpy) was calculated using the Tafel extrapolation method as $CR = (0.13 \times Icorr \times E.W.)/d$, where $Icorr$ is the corrosion current density in µA/cm$^2$, $E.W.$ is the equivalent weight of the corroding species, which is 25.59 for AISI 52100 steel, and $d$ is the density of corroding species, which is 7.81 g/cm$^3$ for AISI 52100 steel. The corrosion rates obtained for [P6,6,6,14][Sali], [P6,6,6,14][Benz], and water were 0.052 ± 0.005, 0.112 ± 0.028, and 3.56 ± 1.216 mpy, respectively. This confirms that the corrosion of steel by the ionic liquids was significantly lower than by water.

The CPDP results for the two ILs are shown in Fig. 5, where horizontal lines identify the key parameters: pitting potential ($E_{pit}$), corrosion potential ($E_{corr}$), and protection potential ($E_p$). As shown in Fig. 5 and Table 1, $E_{pit}$ is lower for [P6,6,6,14][Benz] than [P6,6,6,14][Sali], indicating the steel is more susceptible to the initiation of corrosion pits in the presence of the [Benz]-containing IL. However, for [P6,6,6,14][Benz], $E_p$ is above $E_{corr}$ with a negative hysteresis loop, indicating that the passive film damage repaired itself during the cathodic polarization phase such that further pitting was not initiated [66]. Negative hysteresis typically occurs in CPDP when, for the reverse voltage sweep, the current density goes lower than the forward cycle [67] (indicated by the purple arrows in Fig. 5(a)). As a result, the $E_p$ stays above the $E_{corr}$. In contrast, positive hysteresis occurs when the current density in the reverse cycle becomes more than the first cycle, depicting $E_p < E_{corr}$ [67]. As observed in Fig. 5(b), $E_p$ is below $E_{corr}$ for [P6,6,6,14][Sali] with a positive hysteresis loop, indicating a lack of effective protection or insufficient formation of a protective film to prevent pitting propagation.

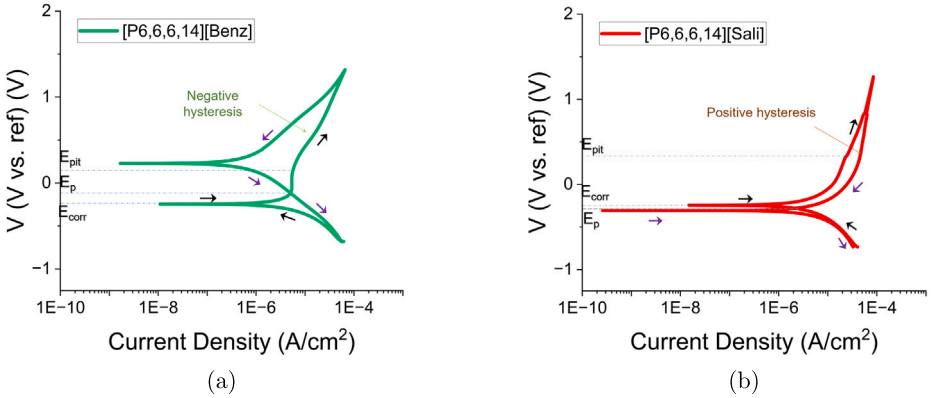


**Fig. 5.** Representative cyclic potentiodynamic polarization curves for (a) [P6,6,6,14][Benz] and (b) [P6,6,6,14][Sali] with black arrows indicating forward scan and purple arrows for the reverse scan. Each test was repeated twice.

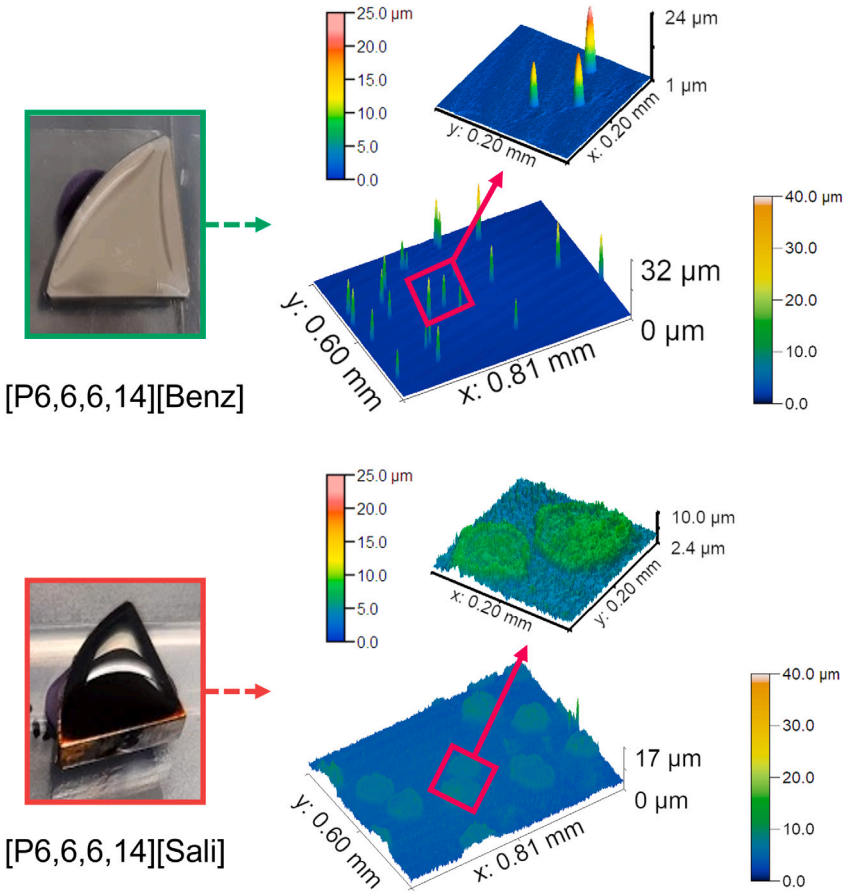


**Fig. 6.** Photos and inverted topography images of steel from the experimental corrosion test for [P6,6,6,14][Benz] and [P6,6,6,14][Sali] on AISI 52100 steel at room temperature after four weeks. The color scale is inverted in the topography images such that large positive values correspond to deep pits.

The results from the CDPD tests indicated the two ILs should have different pitting behavior on steel. Next, a long duration corrosion study was carried out to directly observe pitting. Photos and surface topography images of the steel surfaces after the experimental corrosion tests with [P6,6,6,14][Benz] and [P6,6,6,14][Sali] after four weeks are shown in Fig. 6. With both ILs, pits formed on the surfaces due to corrosion and it was observed that both surfaces got rougher. The average surface roughness, 0.16 µm before testing, increased to 0.92 µm for [P6,6,6,14][Sali] and 0.22 µm for [P6,6,6,14][Benz]. There are also distinct differences in the surface morphologies, with narrow deep pits observed for [P6,6,6,14][Benz] and broad shallow pits for [P6,6,6,14][Sali]. In the case of [P6,6,6,14][Benz], the average maximum roughness valley depth (Rvm) was 18.94 ± 4.41 µm but only about 0.2% of the surface area was pitted. In the case of [P6,6,6,14][Sali], the average depth of the pits was much less, with an Rvm of 2.23 ± 0.58 µm, but the pit area was much larger, covering 11.9% of the surface. The deep purple color for the case of [P6,6,6,14][Sali] indicates the formation of iron-salicylate [68].

Fig. 7 shows the Nyquist plots for the studied ILs. For both ILs, the curve contains a semi-circle representing the charge transfer process, and an upward line, representing the diffusion control process [69]. The wider semi-circle for [P6,6,6,14][Sali] indicates a slower charge

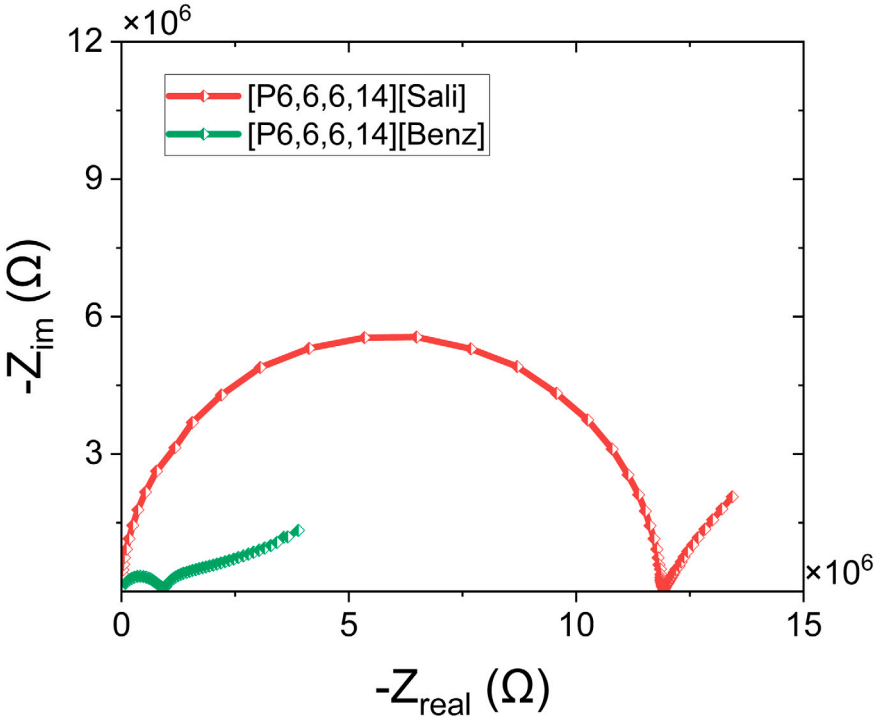


**Fig. 7.** Representative Nyquist plot from the electrochemical impedance spectroscopy for the two ILs. Each test was repeated three times.

transfer process than [P6,6,6,14][Benz]. This could be attributed to the smaller and symmetric anion shape of benzoate, that vertically orients onto the surface, allowing more ions (cation and anion) to come close to the surface [70] and participate in charge transfer. As a result, the charge transfer for [P6,6,6,14][Benz] was likely to be higher than [P6,6,6,14][Sali]. Higher charge transfer increases the molecular adsorption on metal [71]. Possibly for this reason, [P6,6,6,14][Benz] was better able to passivate the surface than [P6,6,6,14][Sali]. The linear portion in the Nyquist plot indicates a diffusion control reaction, meaning the ions are diffused towards the steel surface due to the concentration gradient [72]. Both [P6,6,6,14][Sali] and [P4,4,4,14][Benz] exhibited diffusion, which could have facilitated electron or proton transfer reactions at the interface [73].

To understand any chemical change to the ILs after the long term corrosion test, FTIR analysis was done. Fig. 8 shows the FTIR analysis of the ionic liquids before and after the long-term corrosion tests. Fig. 8 shows that no significant change occurred for [P6,6,6,14][Benz] after corrosion (indicated with a C in Fig. 8). However, some deviations in the FTIR spectra were identified for [P6,6,6,14][Sali]. Particularly, two new peaks were observed around 631 $cm^{-1}$ and 1616 $cm^{-1}$, indicating the presence of iron oxide from the surface due to the dissolution of iron in the presence of the IL.

To characterize changes to the steel surface after the long-term corrosion test in the presence of ILs, Raman spectroscopy was carried out. In Fig. 9, [P6,6,6,14][Sali] exhibits prominent peaks at around 294, 410, 609, 705, and 1315 $cm^{-1}$. These peaks correspond to $Fe_2O_3$ as reported in the literature [74]. The peak at 861 $cm^{-1}$ corresponds to C-O-C, which could be due to the interaction of oxygen on the anionic moiety with the carbon present in the carbon steel [75]. The peak at 1026 $cm^{-1}$ could be for the C-H stretch due to the interaction of cationic alkyl moiety adsorbed chemically on the surface [76]. Similar peaks were obtained with weaker intensity for [P6,6,6,14][Benz] as well. It could be concluded that salicylate, having more oxygen in the hydroxyl group, was able to react with surface more and provide more oxides than benzoate.

The very different types of pitting in the long duration corrosion tests with the two ILs can be understood in terms of the results from the OCP, PDP, and CPDP tests. The OCP and PDP tests showed that the current density and the corrosion rate were higher for [P6,6,6,14][Benz] than [P6,6,6,14][Sali]. Besides, the CPDP results showed that the pitting potential was lower for [P6,6,6,14][Benz]. However, with [P6,6,6,14][Benz], there was sufficient protection by the passive film on steel to limit pitting propagation. Therefore, while corrosion was likely to happen more rapidly with [P6,6,6,14][Benz], the protective film impeded propagation such that subsequent corrosion occurred near the points of initiation, leading to narrow, deep pits. In contrast, while the corrosion rate was slower for [P6,6,6,14][Sali], there was an insufficient protective film such that corrosion propagated on the surface, resulting in broad, but shallower pits.

To better understand the IL interactions with the steel surface at high temperature, PDP experiments were carried out at 373 K. Fig. S3(a–b) shows the PDP curves for [P6,6,6,14][Sali] and [P6,6,6,14][Benz] at room temperature (298 K) and a higher temperature (373 K). For both ILs, the PDP graph shifted to the right at the higher temperature. The corrosion current densities at 373 K for [P6,6,6,14][Sali] and [P6,6,6,14][Benz] are 4.9 $\mu A/cm^2$ and 2.3 $\mu A/cm^2$, respectively. As calculated from two repeated tests, the corrosion rate associated with [P6,6,6,14][Sali] at 373 K is 2.37 ± 0.131, which is faster than at room temperature. Similarly, at the higher temperature, a faster corrosion rate of 0.813 ± 0.362 was observed for [P6,6,6,14][Benz]. At high temperatures, the surface oxidation rate increased and, therefore, the corrosion rate increased as well [77].

Due to their limited time and size scale, reactive MD simulations cannot explicitly model material removal through corrosion. However, as a first step, simulations were used to understand how the ions interact and chemically react with a ferrous surface. First, we analyzed the bonding between surface Fe atoms and the cations and anions in the ILs. As shown in Fig. 10, the surface bonding increased with temperature, as expected since more thermal energy facilitates bond dissociation and formation. There are more cation-Fe bonds than anion-Fe bonds because there is a greater number of atoms in the cations than the anions. However, the difference between Fe-cation bonding for the two ILs was negligible in Fig. 10(a), as expected since the cation is the same. In contrast, the comparison of anion-surface interactions in Fig. 10(b) shows that the key difference between the ILs is that [Sali] exhibits more bonding with the surface than [Benz] at any temperature.

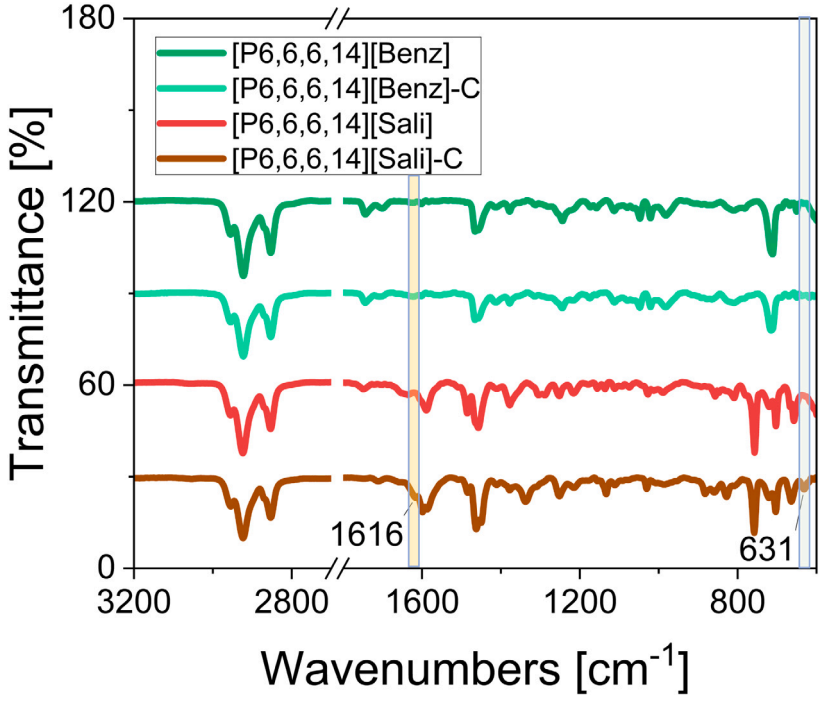


**Fig. 8.** FTIR spectroscopy of the ILs before and after the long duration corrosion tests (C indicates the IL sample after corrosion test).

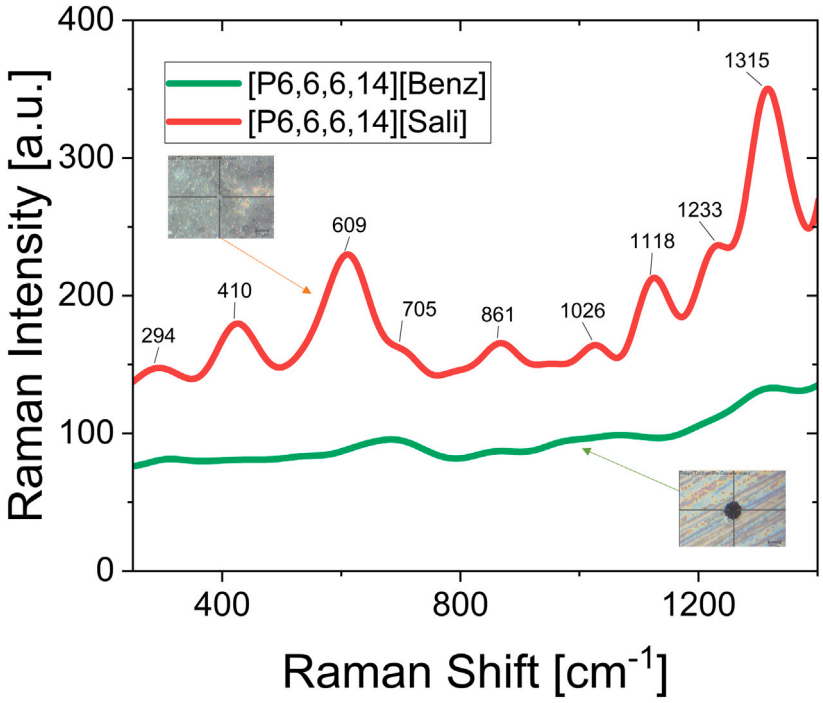


**Fig. 9.** Raman spectroscopy of the surfaces after the long duration corrosion tests. The corroded surface profiles observed using a confocal Raman microscope for [P6,6,6,14][Sali] and [P6,6,6,14][Benz] are shown in the insets.

Therefore, we focused subsequent analysis on interactions between Fe and the anions. Anion chemisorption reactions can occur through formation of either Fe–C or Fe–O bonds. The number of Fe atoms bonded to anion C or O atoms is given in Fig. 11. This analysis shows that bonding with C is dominant for the [Sali] while O bonding is dominant for the [Benz] at all temperatures. Since the reactions with O atoms are the cause of corrosion, the Fe–O bonding was further analyzed, where oxygen atoms are identified by the labels in Fig. 1.

For [Benz], as shown in Fig. 12(a), the number of Fe–O1 and Fe–O2 bonds was similar at all temperatures, as expected since the ion is symmetric. In these simulations, there were only two bonding scenarios: (i) Fe–O1 and Fe–O2 (Fe–O1&O2), or (ii) Fe–O1 or Fe–O2 (Fe–O1||O2).

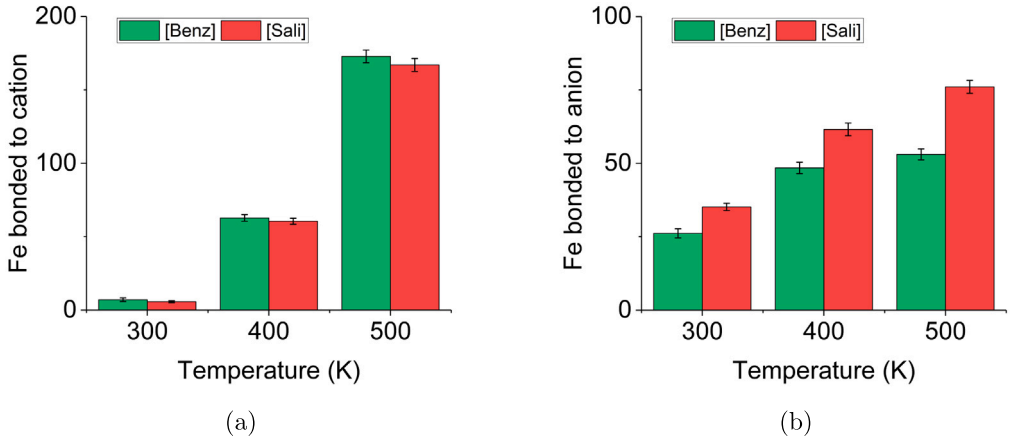


**Fig. 10.** Steady-state number of Fe atoms bonded to (a) cations and (b) anions from simulations of the two ILs interacting with a Fe(100) surface at three different temperatures with error bars showing the standard deviation for three independent tests.

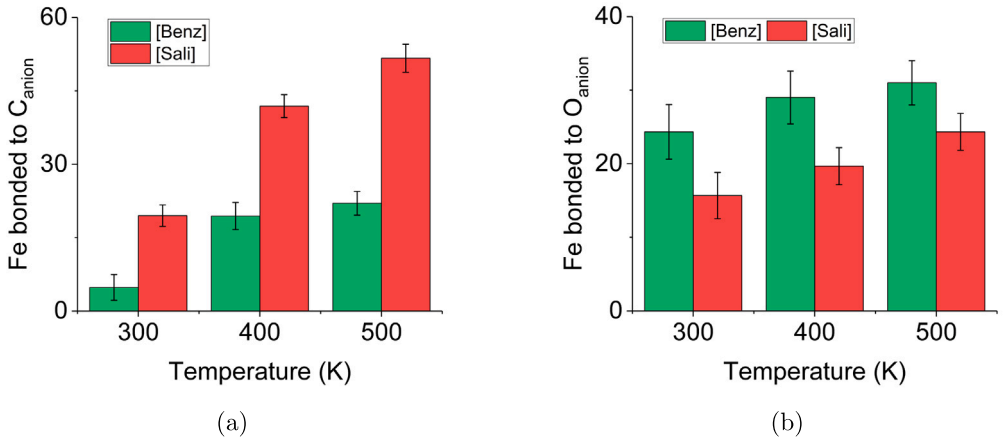


**Fig. 11.** Steady-state number of Fe atoms bonded to (a) C atoms and (b) O atoms in the anions from simulations of the two ILs interacting with a Fe(100) surface at three different temperatures with error bars showing the standard deviation for three independent tests.

Snapshots of representative examples of these two bonding scenarios are shown in Figs. 12(b) and (c). The likelihood of each bonding scenario was calculated from the number of anions exhibiting a given bonding scenario divided by the total number of chemisorbed anions. The calculation was performed at the end of the simulation using data from all three temperatures (no statistical difference between the temperatures was observed). The anion reacted with the surface through Fe–O1&O2 bonding 93.1% of the time, consistent with a previous experimental study that reported bonding at the two O atoms in [Benz] and a $TiO_2$ surface [78]. The Fe–O1‖O2 bonding scenario was only observed 6.9% of the time.

For [Sali], as shown in Fig. 13(a), the reactivity of the O atoms with Fe on the surface decreased as O1 > O2 > O3 at all temperatures. The O1 was more reactive than the O2 in [Sali] due to the presence of the hydroxyl group. As mentioned in a previous study, the hydroxyl group (H–O3) pointing to O2 indicates intramolecular interaction between the H atom in the hydroxyl group and O2, which hinders the ability of O2 to take part in reactions with other atoms [5]. For [Sali], there were four bonding scenarios: Fe–O1&O2, Fe–O1&O2&O3, Fe–O1, and Fe–O3. This is consistent with the multiple possible bonding scenarios for [Sali] on metal surfaces found in previous studies using experiments and simulations showing both the hydroxyl group and carboxyl group can interact with metal [79–83]. Like [Benz], for [Sali], Fe–O1&O2 bonding was the dominant scenario with a probability of 51.9%. This was followed by Fe–O1&O2&O3 with 22.3%, Fe–O1 with 19.1%, and Fe–O3 with 6.7%. In [Sali,] both the carboxyl group and the hydroxyl groups can interact with Fe atoms [84], so there are more possible bonding scenarios for [Sali] than [Benz].

For both [Benz] and [Sali], the key difference between the different bonding scenarios is the orientation of the benzene ring relative to the surface. The orientation of anions has previously been found to affect the interaction between ILs and surfaces. For example, anion orientation was found to affect metal-IL binding energy [70,85], IL film formation on alumina [86], and interactions between ILs and graphene [87]. Therefore, the anion orientation for each Fe–O bonding scenario was analyzed for both ILs.

Anion orientation angle was calculated as the angle between the anion plane (defined by the positions of O1, O2, and the carbon atom in the benzene ring farthest from the carboxyl group), and the plane of the Fe(100) surface. This calculation was performed for each bonding scenario observed in simulations at all three temperatures (no difference in the trends was observed at the different temperatures). As shown in Fig. 14, the anions with Fe–O1&O2 bonding tended to be orientated more vertically (angles approaching 90°) than the other bonding scenarios for both anions. The frequency of Fe–O1&O2 bonding scenario was much higher for [Benz] than [Sali], indicating [Benz] was oriented more vertically relative to the ferrous surface than [Sali]. This is consistent with the dominant O bonding for the [Benz] and dominant C bonding for the [Sali] observed in Fig. 11.

As mentioned previously, reactive MD simulations cannot explicitly model corrosion, so the simulation results cannot directly explain trends observed in the experiments. However, there are some possible

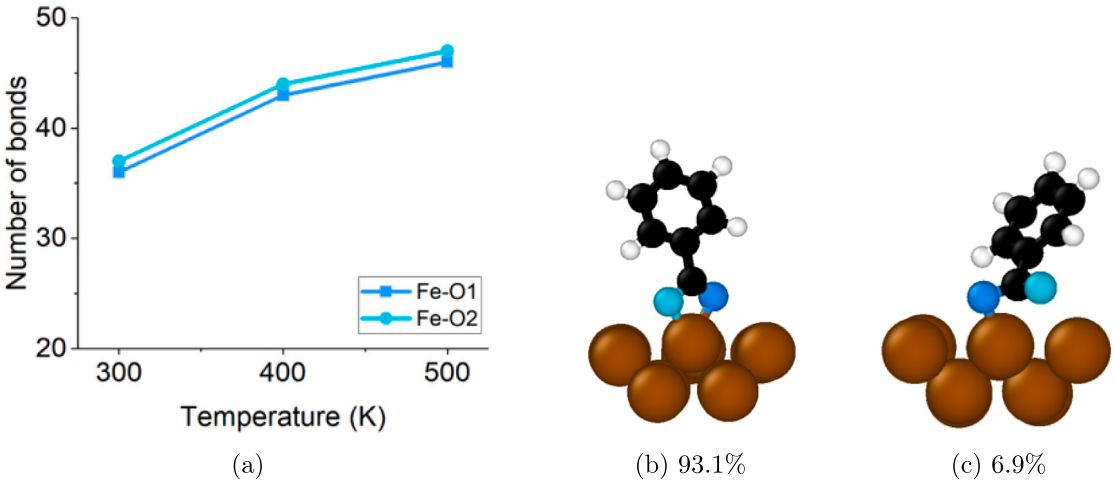


**Fig. 12.** (a) Number of Fe–O1 and Fe–O2 bonds as a function of temperature for [Benz], with representative snapshots of the two possible bonding scenarios (b) Fe–O1&O2 or (c) Fe–O1‖O2, and the percent of all bonded anions in which each scenario was observed.

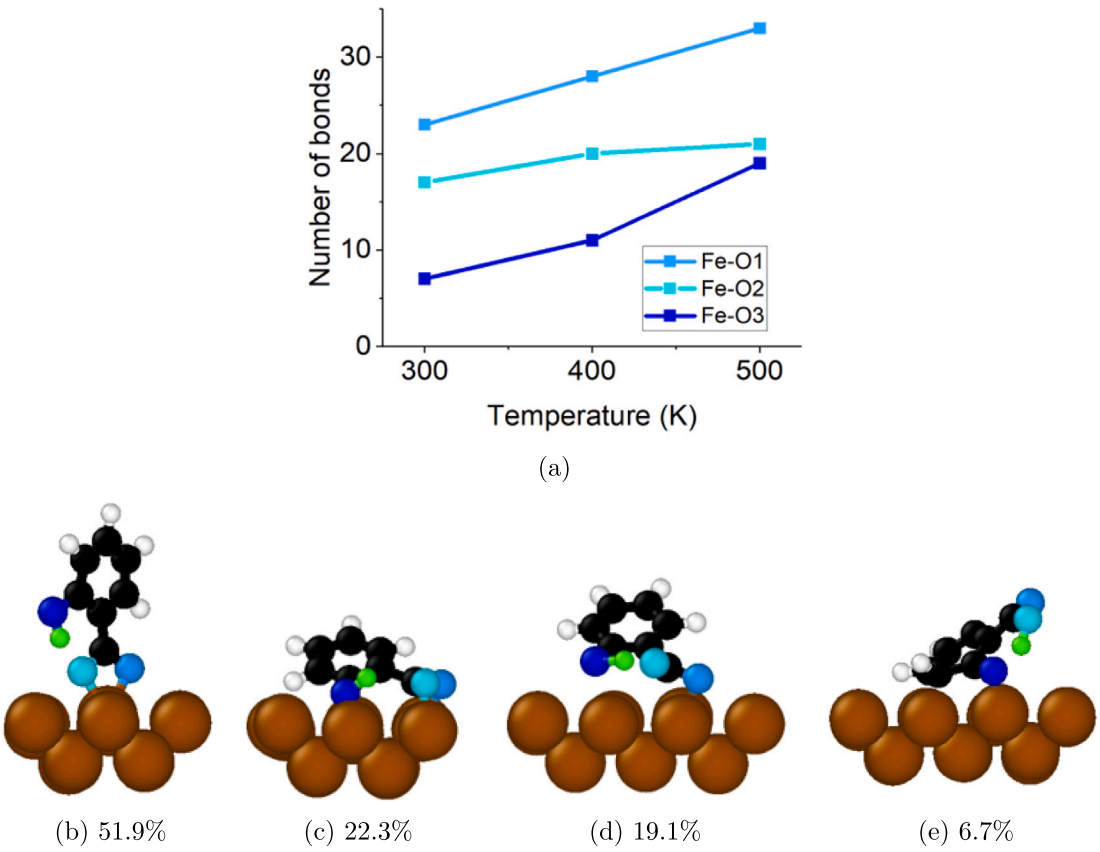


**Fig. 13.** (a) Number of Fe–O1, Fe–O2, and Fe–O3 bonds as a function of temperature for [Sali] with representative snapshots of the four possible bonding scenarios (b) Fe–O1&O2, (c) Fe–O1&O2&O3, (d) Fe–O1 or (e) Fe–O3, and the percent of all bonded anions in which each scenario was observed.

implications of the findings from the simulations for corrosion. First, the vertical orientation of [Benz] anions enabled more [Benz] anions to reach the surface than the [Sali]. This was confirmed by calculating the average anion number density (number of ions per $nm^2$) chemisorbed on the surface, which was found to be 0.42, 0.58, and 0.62 for [Benz] and 0.25, 0.39, and 0.41 for [Sali] at the three different temperatures. A previous study also reported that [Benz] can be absorbed more easily on ferrous surfaces compared to [Sali] [84]. The higher anion number density of [Benz] can lead to a faster rate of charge transfer at the metal/IL interface, supporting the observation in the Nyquist plots. This may suggest a mechanism to explain the higher OCP voltage magnitude in Fig. 3 and higher PDP current flow in Fig. 4 for [P6,6,6,14][Benz] than [P6,6,6,14][Sali].

Second, the orientation of the ions on the surface affects the stability of the Fe-anion complexes formed. It has been reported previously that Fe–[Sali] complexes are stronger and more stable than Fe–[Benz] complexes [84]. Here, the relative stability of the two anions on the surface was estimated using the Fe–O bond order available from ReaxFF [88]. The results in Fig. 15(a) show that the bond order was consistently higher for [Sali], indicating stronger bonds and greater stability of

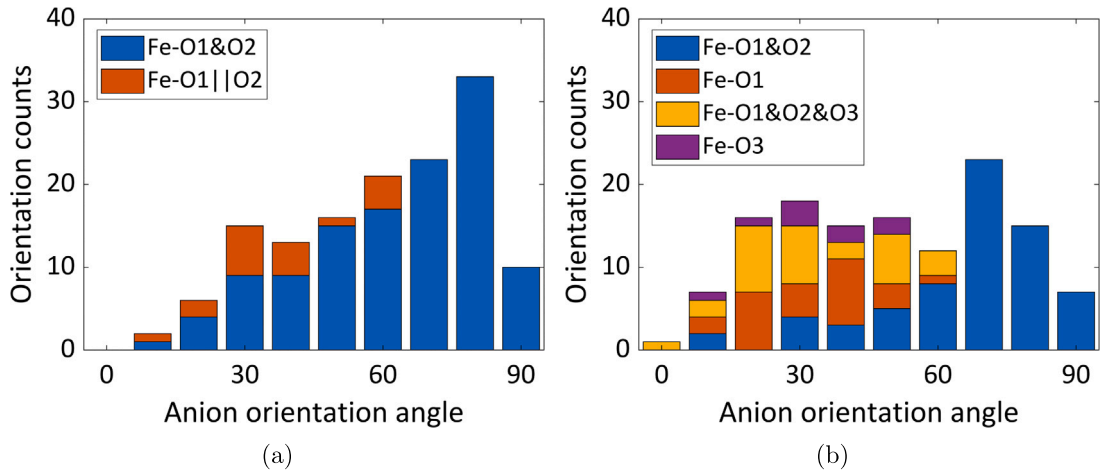


**Fig. 14.** Distribution of the anion orientation angle relative to the surface (at 0°, the benzene ring is parallel to the surface and at 90°the ring is perpendicular to the surface) for the different Fe–O bonding scenarios exhibited by (a) [Benz] and (b) [Sali].

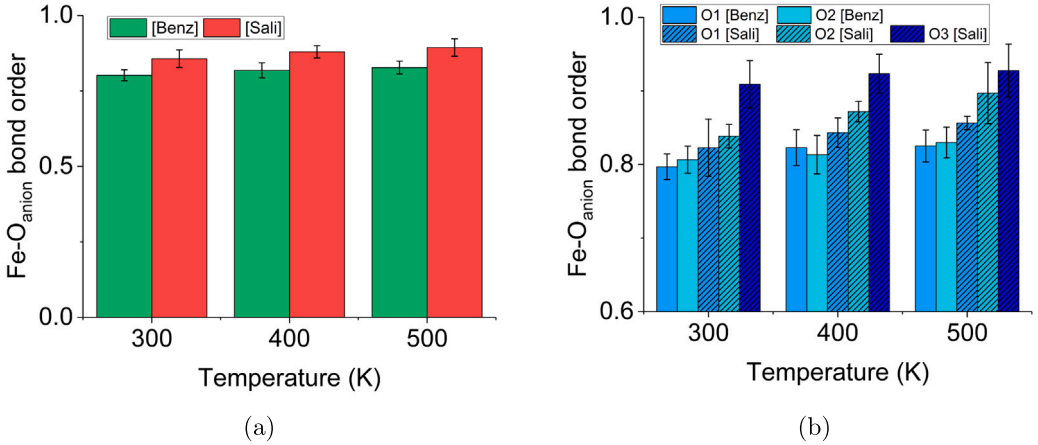


**Fig. 15.** Steady-state Fe–O bond order (a) for the two anions and (b) separated by O type at three different temperatures with error bars showing the standard deviation for three independent tests.

the Fe–[Sali] complex. The bond order analysis was repeated for each oxygen atom separately and, as shown in Fig. 15(b), the strongest Fe–[Sali] bonds were for O3. This bonding site was not available in [Benz], leading to lower chemical stability of the Fe–[Benz] complex. This can be correlated to the FTIR results in Fig. 8 where the peak shape for benzoate did not change whereas, for salicylate, additional peaks for iron oxide were detected, which indicates the formation of the iron oxide-salicylate complex. These analyses of stability may suggest a mechanism to explain the qualitative differences between the ILs in the long-duration corrosion tests in Fig. 6. Since Fe–[benz] complexes are relatively unstable chemically, they are more likely to dissociate, promoting dissolution of the surface and making available new active sites for subsequent corrosion reactions. The dissolution of the ferrous surface is localized around the initial Fe–O bonding leading to, over time, the formation of deep and narrow corrosion pits. In contrast, the stability of the Fe–[Sali] complexes hinders localized dissolution and leads to subsequent bonding and dissolution over a larger area, resulting in the formation of wider and shallower corrosion pits.

## 4. Conclusions

Reactive MD simulations of chemical adsorption and experimental corrosion tests were used to explore the interactions between ferrous surfaces and phosphonium benzoate or phosphonium salicylate. From experiments, both ILs showed much less corrosion of steel than water. However, OCP, PDP, and surface topography analysis showed that the corrosion behavior of the two ILs differed, where corrosion was likely to be faster and form narrower, deeper corrosion pits for the [Benz]-based IL. Further, EIS and CPDP analyses showed that the charge transfer at the interface was higher for [Benz], and its protection potential was higher than [Sali], meaning the surface was passivated and then the passive film protected the surface from further localized pitting. In contrast, [Sali] experienced slower charge transfer, indicating that the passive film broke down to initiate more pits, creating a shallower, but wider pit pattern than [Benz]. While the reactive MD simulations could not directly mimic these experiments, as a first step towards understand mechanisms, the simulations were used to investigate IL-surface interactions. The key observations were that the interactions between Fe and [Benz] were localized at the O atoms in the carboxyl group leading to preferentially vertical alignment relative to the surface. In contrast, the interactions between Fe and [Sali] were distributed across the anion such that [Sali] had more possible bonding scenarios and tended to be oriented parallel to the surface.

Both experiments and simulations confirm that the anion plays a critical role in affecting how ILs react with surfaces, including as part of corrosion processes. The sensitivity of these interactions to the anion is emphasized by the fact that the chemical difference between [Benz] and [Sali] is so subtle. For these two anions particularly, the reactive simulations showed that the orientation of the anion after bonding to the surface can directly affect chemisorption reactions. This has

implications for understanding corrosion mechanisms as well as other scientific and engineering process that involve ionic liquids in contact with ferrous surfaces. Lastly, although the current study was focused on the role of anion moiety and only one surface, the simulation method developed may be used in future work to explore the potential effects of surface inclusions, different metals or surfaces, impurities in the ILs, or solvents molecules on interactions and reactions between ILs and surfaces.

## CRediT authorship contribution statement

**Ting Liu:** Investigation, Writing – original draft. **Md Hafizur Rahman:** Investigation, Writing – original draft. **Pradeep L. Menezes:** Supervision. **Ashlie Martini:** Supervision, Writing – review & editing.

## Declaration of competing interest

The authors declare that they have no known competing financial interests or personal relationships that could have appeared to influence the work reported in this paper.

## Data availability

Data will be made available on request.

## Acknowledgments

The authors acknowledge the support of the National Science Foundation, United States (Grant No. CMMI-2010205 and 2010584). The authors also appreciate valuable input from Dr. Manish Patel.

## Appendix A. Supplementary data

Supporting Information provides additional analysis from experiments. Contents include representative FTIR spectroscopy of [P6,6,6,14][Benz] and [P6,6,6,14][Sali], $^{1}$H NMR spectra for [P6,6,6,14][Benz] and [P6,6,6,14][Sali], and representative potentiodynamic polarization curves for the two ILs at room temperature and at 373 K.

Supplementary material related to this article can be found online at https://doi.org/10.1016/j.corsci.2023.111734.

## References

[1] Z. Lei, B. Chen, Y.-M. Koo, D.R. MacFarlane, Introduction: ionic liquids, Chem. Rev. 117 (10) (2017) 6633–6635.
[2] S.K. Singh, A.W. Savoy, Ionic liquids synthesis and applications: An overview, J. Mol. Liq. 297 (2020) 112038.
[3] M.D. Joshi, J.L. Anderson, Recent advances of ionic liquids in separation science and mass spectrometry, RSC Adv. 2 (13) (2012) 5470–5484.
[4] A.J. Greer, J. Jacquemin, C. Hardacre, Industrial applications of ionic liquids, Molecules 25 (21) (2020) 5207.
[5] A. Khajeh, M.H. Rahman, T. Liu, P. Panwar, P.L. Menezes, A. Martini, Thermal decomposition of phosphonium salicylate and phosphonium benzoate ionic liquids, J. Mol. Liq. 352 (2022) 118700.
[6] J.P. Hallett, T. Welton, Room-temperature ionic liquids: solvents for synthesis and catalysis. 2, Chem. Rev. 111 (5) (2011) 3508–3576.
[7] K.N. Marsh, J.A. Boxall, R. Lichtenthaler, Room temperature ionic liquids and their mixtures—a review, Fluid Phase Equilib. 219 (1) (2004) 93–98.
[8] J. Qu, D.G. Bansal, B. Yu, J.Y. Howe, H. Luo, S. Dai, H. Li, P.J. Blau, B.G. Bunting, G. Mordukhovich, et al., Antiwear performance and mechanism of an oil-miscible ionic liquid as a lubricant additive, ACS Appl. Mater. Interfaces 4 (2) (2012) 997–1002.
[9] J.G. McDaniel, A. Verma, On the miscibility and immiscibility of ionic liquids and water, J. Phys. Chem. B 123 (25) (2019) 5343–5356.
[10] M.H. Rahman, A. Khajeh, P. Panwar, M. Patel, A. Martini, P.L. Menezes, Recent progress on phosphonium-based room temperature ionic liquids: Synthesis, properties, tribological performances and applications, Tribol. Int. 167 (2022) 107331.
[11] S.I. Abu-Eishah, Ionic liquids recycling for reuse, in: Ionic Liquids-Classes and Properties, Rijeka InTech, 2011, pp. 239–272.
[12] N.L. Mai, K. Ahn, Y.-M. Koo, Methods for recovery of ionic liquids—A review, Process Biochem. 49 (5) (2014) 872–881.
[13] Y. Zhou, J. Qu, Ionic liquids as lubricant additives: a review, ACS Appl. Mater. Interfaces 9 (4) (2017) 3209–3222.
[14] A.K. Kasar, C.J. Reeves, P.L. Menezes, The effect of particulate additive mixtures on the tribological performance of phosphonium-based ionic liquid lubricants, Tribol. Int. 165 (2022) 107300.
[15] M. Sivapragasam, J.R. Jaganathan, J.-M. Levêque, M. Moniruzzaman, M.A. Mutalib, Microbial biocompatibility of phosphonium-and ammonium-based ionic liquids, J. Mol. Liq. 273 (2019) 107–115.
[16] A. Hajipour, F. Rafiee, Basic ionic liquids. A short review, J. Iran. Chem. Soc. 6 (4) (2009) 647–678.
[17] S.K. Singh, Solubility of lignin and chitin in ionic liquids and their biomedical applications, Int. J. Biol. Macromol. 132 (2019) 265–277.
[18] C.J. Reeves, A. Siddaiah, P.L. Menezes, Ionic liquids: a plausible future of bio-lubricants, J. Bio- Tribo-Corros. 3 (2) (2017) 18.
[19] T. Welton, Ionic liquids: a brief history, Biophys. Rev. 10 (3) (2018) 691–706.
[20] C. Verma, S.H. Alrefaee, M. Quraishi, E.E. Ebenso, C.M. Hussain, Recent developments in sustainable corrosion inhibition using ionic liquids: A review, J. Mol. Liq. 321 (2021) 114484.
[21] S. Koutsoukos, F. Philippi, F. Malaret, T. Welton, A review on machine learning algorithms for the ionic liquid chemical space, Chem. Sci. 12 (20) (2021) 6820–6843.
[22] T. Liu, P. Panwar, A. Khajeh, M.H. Rahman, P.L. Menezes, A. Martini, Review of molecular dynamics simulations of phosphonium ionic liquid lubricants, Tribol. Lett. 70 (2) (2022) 1–24.
[23] M.H. Rahman, T. Liu, T. Macias, M. Misra, M. Patel, A. Martini, P.L. Menezes, Physicochemical and tribological comparison of bio-and halogen-based ionic liquid lubricants, J. Mol. Liq. (2022) 120918.
[24] C. Gabler, C. Tomastik, J. Brenner, L. Pisarova, N. Doerr, G. Allmaier, Corrosion properties of ammonium based ionic liquids evaluated by SEM-EDX, XPS and ICP-OES, Green Chem. 13 (10) (2011) 2869–2877.
[25] Y. Ma, F. Han, Z. Li, C. Xia, Corrosion behavior of metallic materials in acidic-functionalized ionic liquids, ACS Sustain. Chem. Eng. 4 (2) (2016) 633–639.
[26] M. Zunita, D. Wahyuningrum, Buchari, B. Bundjali, I.G. Wenten, R. Boopathy, Corrosion inhibition performances of imidazole derivatives-based new ionic liquids on carbon steel in brackish water, Appl. Sci. 10 (20) (2020) 7069.
[27] H. Su, L. Wang, Y. Wu, Y. Zhang, J. Zhang, Insight into inhibition behavior of novel ionic liquids for magnesium alloy in NaCl solution: Experimental and theoretical investigation, Corros. Sci. 165 (2020) 108410.
[28] M. Deyab, Q. Mohsen, Understanding the anticorrosion mechanism of phosphonium based ionic liquid for steel in brine water containing $H_2S$ and $CO_2$, J. Mol. Liq. 321 (2021) 114921.
[29] X. Zeng, X. Zheng, L. Guo, Q. Xu, H. Huang, B. Tan, Three imidazole ionic liquids as green and eco-friendly corrosion inhibitors for mild steel in sulfuric acid medium, J. Mol. Liq. 324 (2021) 115063.
[30] M. Mobin, R. Aslam, R. Salim, S. Kaya, An investigation on the synthesis, characterization and anti-corrosion properties of choline based ionic liquids as novel and environmentally friendly inhibitors for mild steel corrosion in 5% HCl, J. Colloid Interface Sci. 620 (2022) 293–312.
[31] Q. Yu, C. Zhang, R. Dong, Y. Shi, Y. Wang, Y. Bai, J. Zhang, M. Cai, F. Zhou, Novel N, P-containing oil-soluble ionic liquids with excellent tribological and anti-corrosion performance, Tribol. Int. 132 (2019) 118–129.
[32] H. Su, Y. Wu, Y. Zhang, Y. Jiang, Y. Ding, L. Wang, J. Zhang, Enhancing the long-term anti-corrosion property of Mg alloy by quaternary phosphonium salt: Integrated experimental and theoretical approaches, Corros. Sci. 178 (2021) 109010.
[33] M. Deyab, Q. Mohsen, Impact of phosphonium-based ionic liquid on the corrosion control of aluminum alloy AA5052 in MED desalination plants during acid cleaning process, J. Mol. Liq. 334 (2021) 116121.
[34] C. Verma, E.E. Ebenso, M. Quraishi, Ionic liquids as green and sustainable corrosion inhibitors for metals and alloys: an overview, J. Mol. Liq. 233 (2017) 403–414.
[35] M. Zunita, Y.J. Kevin, Ionic liquids as corrosion inhibitor: from research and development to commercialization, Results Eng. (2022) 100562.
[36] S. Gurjar, S.K. Sharma, A. Sharma, S. Ratnani, Performance of imidazolium based ionic liquids as corrosion inhibitors in acidic medium: A review, Appl, sur. Sci. Adv. 6 (2021) 100170.
[37] E.K. Ardakani, E. Kowsari, A. Ehsani, S. Ramakrishna, Performance of all ionic liquids as the eco-friendly and sustainable compounds in inhibiting corrosion in various media: A comprehensive review, Microchem. J. 165 (2021) 106049.
[38] M. Uerdingen, C. Treber, M. Balser, G. Schmitt, C. Werner, Corrosion behaviour of ionic liquids, Green Chem. 7 (5) (2005) 321–325.
[39] B. Dilasari, Y. Jung, J. Sohn, S. Kim, K. Kwon, Review on corrosion behavior of metallic materials in room temperature ionic liquids, Int. J. Electrochem. Sci. 11 (1) (2016) 1482–1495.
[40] I. Perissi, U. Bardi, S. Caporali, A. Lavacchi, High temperature corrosion properties of ionic liquids, Corros. Sci. 48 (9) (2006) 2349–2362.

[41] K. Wu, X. Zhou, X. Wu, B. Lv, G. Jing, Z. Zhou, Understanding the corrosion behavior of carbon steel in amino-functionalized ionic liquids for $CO_2$ capture assisted by weight loss and electrochemical techniques, Int. J. Greenhouse Gas Control 83 (2019) 216–227.

[42] L. Pisarova, C. Gabler, N. Dörr, E. Pittenauer, G. Allmaier, Thermo-oxidative stability and corrosion properties of ammonium based ionic liquids, Tribol. Int. 46 (1) (2012) 73–83.

[43] Y.-C. Wang, T.-C. Lee, J.-Y. Lin, J.-K. Chang, C.-M. Tseng, Corrosion properties of metals in dicyanamide-based ionic liquids, Corros. Sci. 78 (2014) 81–88.

[44] B. Dilasari, Y. Jung, K. Kwon, Comparative study of corrosion behavior of metals in protic and aprotic ionic liquids, Electrochem. Commun. 73 (2016) 20–23.

[45] L.T. Popoola, Progress on pharmaceutical drugs, plant extracts and ionic liquids as corrosion inhibitors, Heliyon 5 (2) (2019) e01143.

[46] Q. Zhang, Y. Hua, Corrosion inhibition of mild steel by alkylimidazolium ionic liquids in hydrochloric acid, Electrochim. Acta 54 (6) (2009) 1881–1887.

[47] Y. Qiang, S. Zhang, L. Guo, X. Zheng, B. Xiang, S. Chen, Experimental and theoretical studies of four allyl imidazolium-based ionic liquids as green inhibitors for copper corrosion in sulfuric acid, Corros. Sci. 119 (2017) 68–78.

[48] Y.L. Kobzar, K. Fatyeyeva, Ionic liquids as green and sustainable steel corrosion inhibitors: Recent developments, Chem. Eng. J. 425 (2021) 131480.

[49] T. Espinosa, J. Sanes, A.-E. Jiménez, M.-D. Bermúdez, Surface interactions, corrosion processes and lubricating performance of protic and aprotic ionic liquids with OFHC copper, Applied Surf. Sci. 273 (2013) 578–597.

[50] A. Westerholt, M. Weschta, A. Bosmann, S. Tremmel, Y. Korth, M. Wolf, E. Schlucker, N. Wehrum, A. Lennert, M. Uerdingen, et al., Halide-free synthesis and tribological performance of oil-miscible ammonium and phosphonium-based ionic liquids, ACS Sustain. Chem. Eng. 3 (5) (2015) 797–808.

[51] K.J. Fraser, D.R. MacFarlane, Phosphonium-based ionic liquids: an overview, Aust. J. Chem. 62 (4) (2009) 309–321.

[52] S. Khazalpour, M. Yarie, E. Kianpour, A. Amani, S. Asadabadi, J.Y. Seyf, M. Rezaeivala, S. Azizian, M.A. Zolfigol, Applications of phosphonium-based ionic liquids in chemical processes, J. Iran. Chem. Soc. 17 (2020) 1775–1917.

[53] C.J. Reeves, A. Siddaiah, P.L. Menezes, Friction and wear behavior of environmentally friendly ionic liquids for sustainability of biolubricants, J. Tribol. 141 (5) (2019).

[54] A.K. Kasar, M.H. Rahman, B. D'Souza, P.L. Menezes, Tribological performance of ionic liquid impregnated porous aluminum borate ceramic, Tribol. Int. 180 (2023) 108219.

[55] R.M. Silverstein, G.C. Bassler, Spectrometric identification of organic compounds, J. Chem. Educ. 39 (11) (1962) 546.

[56] L. Martínez, R. Andrade, E.G. Birgin, J.M. Martínez, PACKMOL: A package for building initial configurations for molecular dynamics simulations, J. Comput. Chem. 30 (13) (2009) 2157–2164.

[57] N.I.N. Haris, S. Sobri, Y.A. Yusof, N.K. Kassim, An overview of molecular dynamic simulation for corrosion inhibition of ferrous metals, Metals 11 (1) (2020) 46.

[58] S. Plimpton, Fast parallel algorithms for short-range molecular dynamics, J. Comput. Phys. 117 (1) (1995) 1–19.

[59] B. Zhang, A.C. van Duin, J.K. Johnson, Development of a ReaxFF reactive force field for tetrabutylphosphonium glycinate/CO2 mixtures, J. Phys. Chem. B 118 (41) (2014) 12008–12016.

[60] A. Khajeh, X. Hu, K. Mohammadtabar, Y.K. Shin, A.C. Van Duin, S. Berkebile, A. Martini, Statistical analysis of tri-cresyl phosphate conversion on an iron oxide surface using reactive molecular dynamics simulations, J. Phys. Chem. C 123 (20) (2019) 12886–12893.

[61] A. Khajeh, F.H. Bhuiyan, J.-E. Mogonye, R.A. Pesce-Rodriguez, S. Berkebile, A. Martini, Thermal decomposition of tricresyl phosphate on ferrous surfaces, J. Phys. Chem. C 125 (9) (2021) 5076–5087.

[62] D.J. Evans, B.L. Holian, The nose–hoover thermostat, J. Comput. Phys. 83 (8) (1985) 4069–4074.

[63] C. Chinglenthoiba, A. Joseph, P. Mecheri, S. Vandana, Enhanced corrosion resistance of ABS: bamboo fibre electrospun membrane filtered biodiesel, J. Bio-Tribo-Corros. 6 (4) (2020) 1–7.

[64] F.L. Floyd, S. Tatti, T. Provder, Using DC electrochemical techniques to assess the relative corrosiveness of water-based coatings and their ingredients, J. Coat. Technol. Res. 4 (2007) 111–129.

[65] G. Instrument, Electrochemical Techniques for Corrosion Measurement. URL https://www.gamry.com/assets/Uploads/Echem-Corrosion-Measurement.pdf.

[66] W.S. Tait, Electrochemical corrosion basics, in: Handbook of Environmental Degradation of Materials, Elsevier, 2018, pp. 97–115.

[67] S. Esmailzadeh, M. Aliofkhazraei, H. Sarlak, Interpretation of cyclic potentiodynamic polarization test results for study of corrosion behavior of metals: a review, Prot. Met. Phys. Chem. Surf. 54 (2018) 976–989.

[68] R. Pankratz, F. Bandelin, The colorimetric determination of salicylates, J. Am. Pharm. Assoc. 41 (5) (1952) 267–270.

[69] H.H. Hernández, A.R. Reynoso, J.T. González, C.G. Morán, J.M. Hernández, A.M. Ruiz, J.M. Hernández, R.O. Cruz, Electrochemical impedance spectroscopy (EIS): A review study of basic aspects of the corrosion mechanism applied to steels, Electrochem. Imped. Spectrosc. (2020) 137–144.

[70] T. Liu, M.H. Rahman, P.L. Menezes, A. Martini, Effect of ion pair on contact angle for phosphonium ionic liquids, J. Phys. Chem. B 126 (23) (2022) 4354–4363.

[71] R. Otero, A.V. de Parga, J.M. Gallego, Electronic, structural and chemical effects of charge-transfer at organic/inorganic interfaces, Surf. Sci. Rep. 72 (3) (2017) 105–145.

[72] S. Scheiner, C. Hellmich, Stable pitting corrosion of stainless steel as diffusion-controlled dissolution process with a sharp moving electrode boundary, Corros. Sci. 49 (2) (2007) 319–346.

[73] M. Gutman, E. Nachliel, R. Friedman, The mechanism of proton transfer between adjacent sites on the molecular surface, Biochimica et Biophysica Acta (BBA)-Bioenergetics 1757 (8) (2006) 931–941.

[74] P. Kumar, H. No-Lee, R. Kumar, Synthesis of phase pure iron oxide polymorphs thin films and their enhanced magnetic properties, J. Mater. Sci., Mater. Electron. 25 (2014) 4553–4561.

[75] E. Nguyen, A. Chrimes, R. Brkljača, J. Ou, K. Berean, S. Zhuiykov, K. Kalantarzadeh, Assessment of a Raman micro-spectroscopy/microfluidics unit using a model E. coli/glucose bio-system, in: The 7th IEEE International Conference on Nano/Molecular Medicine and Engineering, IEEE, 2013, pp. 157–162.

[76] R. Risi, L. Manti, G. Perna, M. Lasalvia, V. Capozzi, I. Delfino, M. Lepore, X-ray radiation-induced effects in human mammary epithelial cells investigated by Raman microspectroscopy, in: Biophotonics: Photonic Solutions for Better Health Care III, Vol. 8427, SPIE, 2012, pp. 437–446.

[77] V. Konovalova, The effect of temperature on the corrosion rate of iron-carbon alloys, Mater. Today Proc. 38 (2021) 1326–1329.

[78] Q. Guo, I. Cocks, E. Williams, The adsorption of benzoic acid on a $TiO_2$ (110) surface studied using STM, ESDIAD and LEED, Surf. Sci. 393 (1–3) (1997) 1–11.

[79] M. del Arco, S. Gutiérrez, C. Martín, V. Rives, J. Rocha, Synthesis and characterization of layered double hydroxides (LDH) intercalated with non-steroidal anti-inflammatory drugs (NSAID), J. Solid State Chem. 177 (11) (2004) 3954–3962.

[80] M.A. Morosanova, E.I. Morosanova, Silica-titania xerogel for solid phase spectrophotometric determination of salicylate and its derivatives in biological liquids and pharmaceuticals, Chem. Cent. J. 9 (1) (2015) 1–8.

[81] M. Ata, Y. Liu, I. Zhitomirsky, A review of new methods of surface chemical modification, dispersion and electrophoretic deposition of metal oxide particles, RSC Adv. 4 (43) (2014) 22716–22732.

[82] S. Roy, J. Kästner, Synergistic substrate and oxygen activation in salicylate dioxygenase revealed by QM/MM simulations, Angew. Chem., Int. Ed. 55 (3) (2016) 1168–1172.

[83] J.A. Van der Horn, B. Souvignier, M. Lutz, Crystallization, structure determination and reticular twinning in iron (III) salicylate: Fe[(HSal)(Sal)$(H_2O)_2$], Crystals 7 (12) (2017) 377.

[84] R. Bucci, V. Carunchio, A. Girelli, Formation of iron (II) complexes with some aromatic anions in DMSO, Inorg. Chim. Acta 141 (1) (1988) 99–102.

[85] A.C. Mendonça, P. Malfreyt, A.A. Padua, Interactions and ordering of ionic liquids at a metal surface, J. Chem. Theory Comput. 8 (9) (2012) 3348–3355.

[86] M. Sobota, I. Nikiforidis, W. Hieringer, N. Paape, M. Happel, H.-P. Steinruck, A. Gorling, P. Wasserscheid, M. Laurin, J. Libuda, Toward ionic-liquid-based model catalysis: growth, orientation, conformation, and interaction mechanism of the $[Tf_2N]$- anion in [BMIM]$[Tf_2N]$ thin films on a well-ordered alumina surface, Langmuir 26 (10) (2010) 7199–7207.

[87] S. Xu, S. Xing, S.-S. Pei, S. Baldelli, Sum frequency generation spectroscopy study of an ionic liquid at a graphene-$BaF_2$ (111) interface, J. Phys. Chem. B 118 (19) (2014) 5203–5210.

[88] T.P. Senftle, S. Hong, M.M. Islam, S.B. Kylasa, Y. Zheng, Y.K. Shin, C. Junkermeier, R. Engel-Herbert, M.J. Janik, H.M. Aktulga, et al., The ReaxFF reactive force-field: development, applications and future directions, NPJ Comput. Mater. 2 (1) (2016) 1–14.